Sustainable Energy & Fuels

ROYAL SOCIETY OF CHEMISTRY

PAPER

View Article Online
View Journal | View Issue

Cite this: *Sustainable Energy Fuels*, 2023, 7, 1981

Cellulose as sacrificial agents for enhanced photoactivated hydrogen production†

María Isabel Alvarado-Ávila,[a] Stefano De Luca,[a] Ulrica Edlund,[b] Fei Ye [a] and Joydeep Dutta *[a]

The search for new energy sources together with the need to control greenhouse gas emissions has led to continued interest in low-emitting renewable energy technologies. In this context, water splitting for hydrogen production is a reasonable alternative to replace fossil fuels due to its high energy density producing only water during combustion. Cellulose is abundant in nature and as residuals from human activity, and therefore a natural, ecological, and carbon-neutral source for hydrogen production. In the present work, we propose a sustainable method for hydrogen production using sunlight and cellulose as sacrificial agents during the photocatalytic water splitting process. Platinum (Pt) catalyst activates hydrogen production, and parameters such as pH of the system, cellulose concentration, and Pt loading were studied. Using different biomasses, we found that the presence of hemicellulose and xyloglucan as part of the molecular composition considerably increased the H_2 production rate from 36 μmol L^{-1} in one hour for rapeseed cellulose to 167.44 μmol L^{-1} for acid-treated cellulose isolated from *Ulva fenestrata* algae. Carboxymethylation and TEMPO-oxidation of cellulosic biomass both led to more stable suspensions with higher rates of H_2 production close to 225 μmol L^{-1}, which was associated with their water solubility properties. The results suggest that cellulosic biomass can be an attractive alternative as a sacrificial agent for the photocatalytic splitting of water for H_2 production.

Received 29th January 2023
Accepted 15th March 2023

DOI: 10.1039/d3se00109a

rsc.li/sustainable-energy

1. Introduction

According to the International Energy Agency (IEA), global energy demands increased by 4.6% during 2021, overcoming the 4% decline in 2020 due to the economic slowdown attributed to the Covid-19 pandemic.[1] This has led to an increase in the consumption of non-renewable energy sources like coal and fossil fuels, increasing the concentration of carbon dioxide in the atmosphere to over the threshold of 400 ppm. The share of fossil fuels in the global energy mix has been around 80% for decades.[2] Efforts are being made across the globe to replace and reduce the use of fossil fuels by increasing the use of renewable energies from solar photovoltaics to windmills and green H_2 usage, amongst others. Hydrogen is one of the best candidates to replace the use of carbon-based fuels and achieve total decarbonization in maritime transportation,[3] aircraft,[4] road transportation, and in heating of building and manufacturing activities.[5] Not only due to its superior energy density (120 MJ kg^{-1} compared to 44 MJ kg^{-1} of gasoline) but also because the only byproduct of combustion is water which would assist in the reduction of greenhouse gas emission, water splitting for hydrogen production is being extensively studied by researchers.

Several methods to produce hydrogen have been developed over the last decades. The most used commercial process is steam methane reforming, which contributes to 80 to 85% of global hydrogen production, followed by coal gasification and electrolysis.[6–8] Economical and efficient methods to produce hydrogen where renewable energies like solar, wind, and biomass are involved are attracting continued attention. The use of solar energy for hydrogen production is considered the most promising because of being an unlimited resource with irradiation reaching 6 kW h m^{-2}.[9] Water splitting *via* photocatalysis and photo/electro-catalysis began to attract attention since Fujishima and Honda found that titanium dioxide (TiO_2), working as a photoanode, split water in a photo/electrochemical cell even when no current was applied.[10] It is well known that semiconductors like titanium dioxide (TiO_2), cadmium sulfide (CdS), zinc oxide (ZnO), tungsten oxide (WO_3), *etc.*, with band gaps around or lower than 3 eV are suitable for water oxidation allowing oxygen and hydroxyl radical production.[11–13] Photocatalyst stability in water solution is another requirement for its implementations, and hence TiO_2 has been extensively investigated as a photocatalyst due to its

[a]*Functional NanoMaterials Group, Department of Applied Physics, School of Engineering Sciences, KTH Royal Institute of Technology, Hannes Alfvéns väg 12, 114 19 Stockholm, Sweden. E-mail: joydeep@kth.se*

[b]*Fibre and Polymer Technology, KTH Royal Institute of Technology, SE 100 44 Stockholm, Sweden*

† Electronic supplementary information (ESI) available. See DOI: https://doi.org/10.1039/d3se00109a

ability to absorb light mainly in the UV range with exceptional stability in a wide pH range.[14–16]

Nevertheless, to solve the electron–hole recombination problems, incorporating a co-catalyst like metal nanoparticles[17] or another semiconductor[18,19] acting as an electron scavenger to lower the activation barrier for the reaction has been studied.[20–24] On the other hand, the addition of sacrificial agents like sodium sulfide (Na_2S), ethanol (C_2H_5OH), methanol (CH_3OH), and different type of alcohols acting as hole scavengers[25,26] improves the separation of charges.[27] Even though methanol or isopropanol has been extensively used as electron acceptors during the photocatalytic water splitting process,[28,29] it is also a valuable resource and expensive fuel in the industry by itself, limiting its economic viability. Cellulosic biomass is a more reasonable alternative as a sacrificial agent, especially since it is generally considered to be a carbon-neutral emission source where the carbon dioxide absorbed during the plant growth is then released during hydrogen production.[30]

Cellulose is plentiful in human-created residuals like straw, tree branches, wastepaper, cotton waste, fruit peels, *etc.*, making it a sustainable source to produce hydrogen. Lignocellulose represents a major fraction of above 90% of all terrestrial plant biomass (170 billion $\times$ 10^9 tons per annum). Lignocellulosic biomass contains cellulose (38–50%), which is composed of linear chains of β-1,4 linked D-glucose units and is insoluble in water, along with hemicelluloses (23–38%) and lignin (15–25%). The current use of cellulose as a fuel precursor for alcohol, sugar, and hydrogen production is based on complex thermochemical processes like steam gasification, fast pyrolysis, hydrolysis, and fermentation.[31–33] Lignocellulose biomasses can serve as sacrificial agents (electron donors) to reduce e^-–h^+ recombination in a photocatalytic reaction leading to a more efficient process since many organic compounds like alcohols, polyols, sugar as well as organic acids act as electron donors.[34] Electrons in a semiconductor can be excited from the valence band (VB) to the conduction band (CB) upon absorption of photons with energy higher than the band gap. The photo-generated electrons and holes have certain electrical potential and if the potential of the holes is positive enough, they can oxidize water molecules according to two types of reactions shown hereunder:[35]

$$2H_2O \rightarrow O_2 + 4H^+ + 4e^-,\ E^0 = 1.23\ V \quad (1)$$

$$H_2O \rightarrow {}^{\bullet}OH + H^+ + e^-,\ E^0 = 2.73\ V \quad (2)$$

The reactions are reported together with the respective potential *vs.* Standard Hydrogen Electrode (SHE) at which they occur in acidic pH, labeled as E^0. Reaction (1) requires a considerably lower potential than reaction (2). Moreover, while reaction (1) leads to the formation of O_2, reaction (2) leads to the formation of hydroxyl radicals $^{\bullet}OH$. The electrons on the right side of both reactions are captured by holes generated in the VB of the photocatalyst, leaving protons in the medium, while photoexcited electrons are used to reduce such protons according to the following reaction, resulting in the evolution of H_2:

$$2H^+ + 2e^- \rightarrow H_2,\ E^0 = 0\ V \quad (3)$$

The potentials needed for H_2O oxidation and H_2 evolution reactions are affected by the pH of the system.

Photocatalytic degradation of cellulose-containing biomass can be a simple and promising path for hydrogen production by utilizing cellulose and the created intermediates as sacrificial agents, but only a few studies with this approach have been reported in the literature.[36–40] A comprehensive study of the degradation of different types of biomasses with different cellulose, hemicellulose, and lignin concentrations is limited. In this work, we report photocatalytic hydrogen production by using different sources of cellulose and cellulose derivatives as sacrificial agents. TiO_2 and platinum (Pt) were used as a photocatalyst and co-catalyst, respectively. Parameters like pH, Pt loading, and biomass concentration were studied to better understand the hydrogen production mechanism and limitations of using cellulosic biomass as a sacrificial agent.

2. Experimental

2.1. Materials

Titanium dioxide (TiO_2) nanoparticles (commercial P25), sodium dodecylbenzene sulfonate (SDBS), sodium borohydride ($NaBH_4$), sodium hydroxide (NaOH), sodium sulfide nonahydrate ($Na_2S{\cdot}9H_2O$), D-glucose (dextrose), and hexachloroplatinic acid (H_2PtCl_6) were purchased from Sigma Aldrich Chemie GmbH (Taufkirchen, Munich, Germany). Hydrochloric acid (HCl) and nitric acid (HNO_3) were from Merck (Darmstadt, Germany) and terephthalic acid disodium salt (TPA) and 2-hydroxyterephthalic acid (hTPA) from Tokyo Chemical Industry (Zwijndrecht, Belgium). All the chemicals were used as received and aqueous solutions were prepared with deionized water (DI water).

Table 1 shows different types of cellulosic biomasses studied in this work, including bleached and un-bleached lignocellulose extracted from rapeseed straw, α-cellulose from spruce, cellulose extracted from *U. fenestrata* algae, acid-treated cellulose extracted from *U. fenestrata* algae and TEMPO (2,2,6,6-tetramethylpiperidine-1-oxyl radical)-oxidized CNF (cellulose nanofibers). These celluloses were prepared according to the processes described in the references shown in Table 1 except for sodium carboxymethyl cellulose (CMC-Na) that was acquired from Carl Roth, and had an average degree of substitution of 0.8.

2.2. Photocatalyst preparation

As received, P25 TiO_2 was covered with platinum nanoparticles (Pt NPs) following a modified version of the procedure reported by Yao *et al.*[44–46] In brief, 120 mg of sodium dodecylbenzene sulfonate (SDBS) surfactant was dissolved in 30 mL of deionized (DI) water. When the SDBS was completely dissolved, 150 mg of P25 was added under continuous stirring. Finally, a solution of 3 mM hexachloroplatinic acid was prepared, and predetermined volumes were added to obtain different Pt mass loadings on TiO_2. The solution was sonicated for 30 min and

Table 1 List of cellulose samples used as sacrificial agents during the photocatalytic hydrogen production process

Biomass	Carbohydrate and lignin composition	Crystallinity index	Reference
Lignocellulose extracted from rapeseed straw	Cellulose 80% Hemicelluloses 11% Lignin 8%	Not available	41
Lignocellulose extracted from rapeseed straw – H_2O_2 bleached	Cellulose 85% Hemicelluloses 8% Lignin 6%	83%	41
α-Cellulose fibers from spruce pulp	Cellulose 99%	71%	Supplied by Södra Cell AB
Cellulose extracted from *U. fenestrata*	Cellulose 85% Xyloglucan 15%	48%	42
Acid-treated cellulose extracted from *U. fenestrata*	Cellulose 91% Xyloglucan 9%	63%	42
TEMPO-oxidized CNF prepared from never-dried spruce pulp	Cellulose 99%	Not available	43
CMC-Na	The sodium salt of cellulose with carboxymethyl pendant groups, very pure. Degree of substitution = 0.8	Not available	Supplied by Carl Roth

stirred for 1 h at room temperature. Following this, the recipient containing the solution was transferred to an oil bath preheated to 70 °C, and 15.8 mg of $NaBH_4$ was added to reduce the Pt in the solution and thereafter aged for 2 h. Following the aging process, the solution was cooled down to room temperature, centrifuged to recover the photocatalyst, and then rinsed several times with DI water and ethanol prior to further use. Dry powder was obtained by heating overnight at 60 °C in an atmospheric oven and stored for further use. Three photocatalysts were prepared with a Pt loading of 0.2, 0.5, and 1 wt% labeled as 0.2Pt–TiO_2, 0.5Pt–TiO_2 and 1Pt–TiO_2, respectively.

2.3. Characterization

Microstructure and elemental analysis of the photocatalysts were carried out by using a ZEISS Ultra-55 scanning electron microscope (SEM) equipped with energy-dispersive X-ray spectroscopy (SEM-EDX) working at 10 kV. The titanium dioxide and Pt-coated Titanium dioxide nanoparticles were also studied and crystal structure was determined using high resolution transmission electron microscopy (HR-TEM, JEOL JEM-2100F, Akishima, Tokyo). Optical absorption was measured by PerkinElmer Lambda 750 UV/Vis spectrophotometer. Photoluminescence (PL) measurements were used to determine the hydroxyl radicals (˙OH) production using a PerkinElmer LS 55 Fluorescence spectrometer. Hydroxyl radicals were determined using terephthalic acid disodium (TPA) salt as a selective scavenger of ˙OH. TPA reacts with ˙OH producing highly fluorescent 2-hydroxyterephthalic acid (hTPA) that can be determined by PL spectroscopy. In brief, 7.5 mg of the photocatalyst was added to 25 mL of 200 μM TPA solution and magnetically stirred in darkness for 30 min to reach adsorption equilibrium. Nitrogen gas was bubbled for 10 min to remove dissolved oxygen. Then the solution was irradiated with a commercial UVA light source (OSRAM Ultra-Vitalux 300 W lamp) for 30 min, and samples were extracted every 10 minutes. PL measurements were used to determine hTPA concentration using an excitation wavelength of 325 nm (calibration curve for hTPA concentration is provided as Fig. S1 in the ESI†). DelsaNano C was used to determine the zeta potentials and particle size using dynamic light scattering technique. Total Pt loading was determined by digesting the particles in aqua regia and following this, after 50 times dilution, inductively coupled plasma-optical emission spectroscopy (ICP-OES) was used to determine the absolute quantities (Thermo Scientific iCAP 6500).

2.4. Photocatalytic hydrogen production

The experiments were run in a 25 mL three-necked round-bottomed Pyrex glass flask filled with 25 mL of the studied suspension in water with 0.3 mg mL^{-1} of photocatalyst and 0.25 mg mL^{-1} of respective cellulose samples (Table 1). The composition of sacrificial agents varied from 99% cellulose to 85%, with or without the presence of hemicelluloses and lignin. The crystallinity index (CI) measures the relative amount of crystalline cellulose in a two-phase model to describe cellulose chains with crystalline and amorphous regions.[47]

The initial suspension pH was adjusted to 5 using HCl (0.1 M) and NaOH (0.1 M). Before the start of each experiment, the system was sonicated for 30 min and then purged using nitrogen gas for another 30 min to reduce dissolved oxygen. The light source simulating natural sunlight was placed at a distance such that the irradiation flux on the sample was around 1000 W m^{-2}. Hydrogen gas concentration was continuously measured using a H_2 microsensor from Unisense, Denmark. The calibration curve can be found in ESI (Fig. S2†). An external air blower was used to keep the temperature stable. The reactor was sealed with rubber caps, and the sensors were connected directly into the system through syringe probes.

3. Results and discussions

Microstructure of TiO_2 (P25) photocatalyst and TiO_2 with 0.2, 0.5, and 1% Pt loading are shown in Fig. 1. From the SEM micrographs, no clear evidence of the Pt NPs deposition could be observed possibly due to the small sizes. Energy dispersive X-

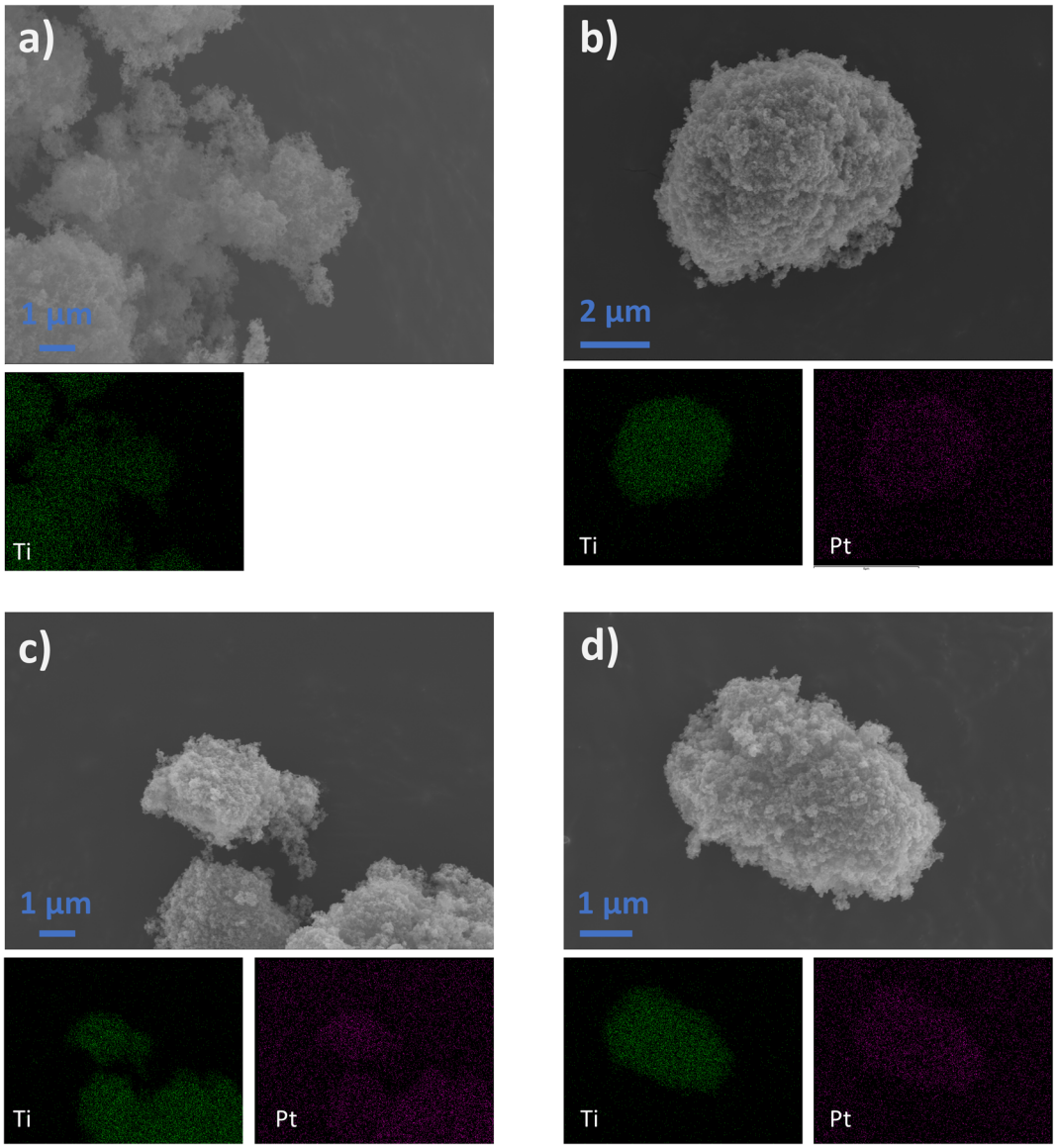

Fig. 1 Scanning Electron Microscopy (SEM) images corresponding to (a) TiO_2 (P25) NPs with their respective EDX spectra below, (b) 0.2% Pt loaded on TiO_2 (P25) (0.2% Pt–TiO_2) and the elemental distribution of Ti and Pt, (c) 0.5% Pt loaded on TiO_2 (P25) (0.5% Pt–TiO_2) and its corresponding EDX spectra for Ti and Pt, and (d) 1% Pt deposited on P25 NPs (1% Pt–TiO_2) with its respective EDX spectra images regarding the distribution of Ti and Pt elements.

ray spectroscopy (EDX) profiles below every micrograph in Fig. 1 however conclusively show Ti and Pt distributions confirming the presence of Pt on titania NPs. In addition, ICP-OES was used to determine the total amount of platinum loading on the TiO_2 during the synthesis process, showing that 0.095, 0.36, and 0.86 wt% of Pt were deposited on 0.2Pt–TiO_2, 0.5Pt–TiO_2 and 1Pt–TiO_2, respectively. All the photocatalysts tested showed a homogeneous platinum distribution on the titanium dioxide substrate attributed to the role of SDBS as an anionic surfactant stabilizing the metal clusters.[44,48] The primary particle size of TiO_2 was noted as 21 nm by the supplier. Hydrodynamic diameter and distribution at different pH of the titania particles measured by DLS are shown in Fig. S3a.† TiO_2 tends to agglomerate at neutral pH forming clusters with sizes around 522 nm and 218 nm. On the other hand, after loading Pt, the diameter of the clusters decreased to 108, 132, and 114 nm when the amount of Pt was 0.2, 0.5, and 1%, respectively. It is well known that the point of zero-charge of TiO_2 is around pH 6.7 to 7.[49,50] This is reflected in Fig. S3b and c,† where the hydrodynamic size decreased drastically in acidic pH, demonstrating that the charge of the particle surface increases preventing the aggregation of the nanoparticles. From Fig. S3a,† it is possible to observe that the incorporation of Pt on the TiO_2 surface prevents aggregation and decreases the hydrodynamic diameter. It has been reported that platinum nanoparticles present a negative surface charge over almost all pH ranges,[51–53] modifying the zero-charge point of the photocatalyst. Fig. S3d† shows the role of SDBS during the platinum deposition on TiO_2,

stabilizing the nanoparticles and narrowing the hydrodynamic particle size distribution.

The morphology of TiO_2 and Pt nanoparticle-coated TiO_2 at different magnifications is shown in Fig. 2. Both the truncated tetrahedral anatase and short-rod-shaped rutile phase of TiO_2 are observed, suggesting that the particles are of mixed anatase and rutile phases (Fig. 2b). Selected-area electron diffraction (SAED) pattern of TiO_2 nanoparticles (Fig. 2c) was used to calculate the interplanar spacings of TiO_2 crystals. The obtained result of *d*-spacing, 0.348 nm, 0.227 nm, 0.185 nm, 0.166 nm, 0.147 nm, and 0.128 nm, can be indexed to anatase (101), rutile (200), anatase (200), (211), (204) and (215) planes,[54] respectively, which proves the major phase of TiO_2 used in this work is anatase with the tetragonal crystal structure. In Fig. 2d, Pt nanoparticles with a size of about 3–5 nm can be clearly observed to be attached on the edge of TiO_2 nanoparticle. A high-resolution image of Fig. 2e further exhibits that the Pt particles grown on TiO_2 have a lattice spacing of ~0.23 nm, which is from the (111) planes of Pt. In the diffraction pattern of 0.5Pt–TiO_2 (Fig. 2f), several diffracted spots were selected to calculate the lattice spacing in real space. The spacings of 0.23 nm and 0.197 nm can be indexed to (111) and (200) planes of face-centered-cubic structured Pt, labeled in Fig. 2f.

The XRD patterns of the prepared samples were obtained to learn about the crystalline phase proportion and the crystallite size of the photocatalysts (see Fig. S4a†). XRD curves of all samples were dominated with peaks belonging to TiO_2 anatase and rutile phases (ICDD file no. 21-1272 and ICDD file no. 21-1276, respectively shown in Fig. S4b†). The phase composition was calculated using the relative intensity method (eqn (4)),[55] where A% corresponds to the weight fraction of the anatase phase, I_R represents the intensity of the strongest peak of the rutile phase (110), and I_A the intensity of the strongest peak if anatase phase corresponding to (101). From this, it was found that anatase represented 85% of all phases and rutile 15% of TiO_2. No evident platinum was registered on loaded TiO_2 samples. The absence of Pt can be ascribed to the small size of Pt NPs and its high dispersion on the TiO_2 particles.[56] Crystallite size was calculated using the Scherrer equation (eqn (5)) where L is the crystallite size, K corresponds to a constant with a value of 0.9, λ is the wavelength of the X-ray used (1.54 Å), θ is the Bragg angle, and FWHM is the full width at half-maximum of the peak, in this case, peaks with the highest intensity were considered for both phases. The crystallite size of the commercial TiO_2 estimated from the rutile and anatase phases was 18.48 nm and 18.40 nm respectively. No changes were found when Pt was loaded on the photocatalyst, indicating that Pt NPs did not affect the crystal structure of TiO_2 (no electronic doping leading to crystal structure changes), and it was only deposited on the surface.

$$A\% = \frac{1}{1 + 1.265\frac{I_R}{I_A}} \times 100 \quad (4)$$

$$L = \frac{K\lambda}{\beta \cos(\theta)} \quad (5)$$

The optical properties of the photocatalyst in terms of adsorption are fundamental in the evaluation of its

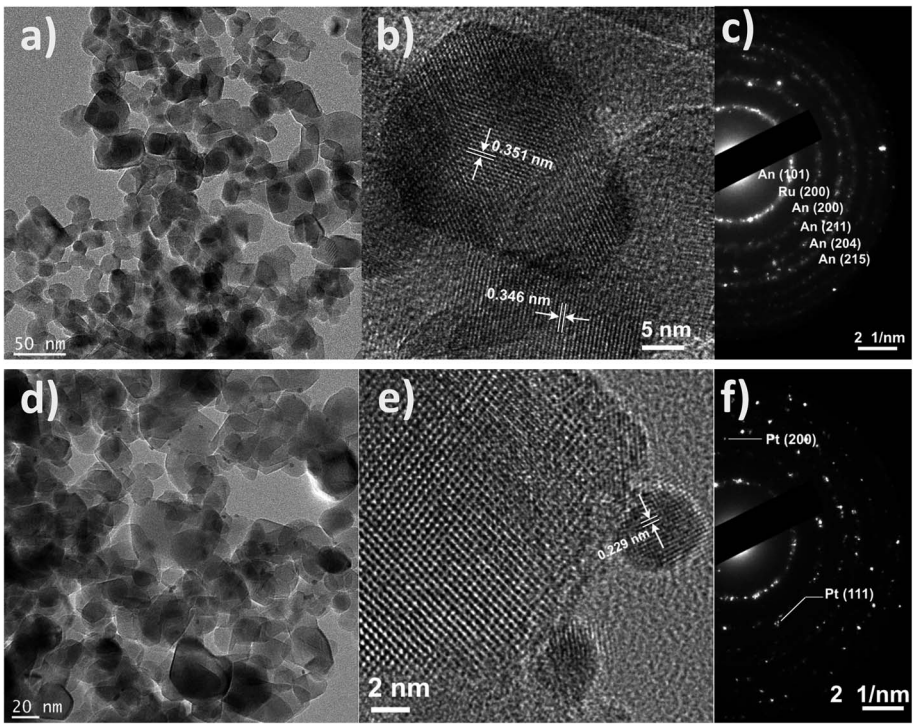

Fig. 2 (a and b) Transmission Electron Microscopy (TEM) images and (c) SAED pattern of TiO_2 nanoparticles; (d and e) TEM images and (f) SAED pattern of Pt nanoparticle-coated TiO_2 nanorods. An: anatase, Ru: rutile.

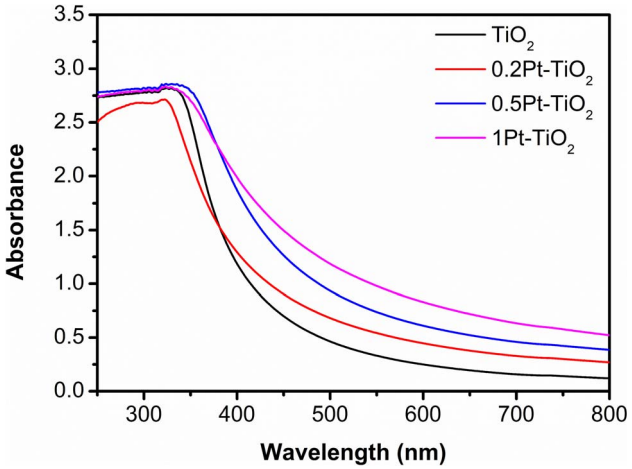

Fig. 3 UV-vis spectra for different photocatalysts, commercial TiO_2, TiO_2 loaded with 0.2 wt% Pt (0.2Pt–TiO_2), 0.5 wt% Pt (0.5Pt–TiO_2), and 1 wt% Pt (0.2Pt–TiO_2).

performance.[57] A strong adsorption in the UV range around 320 nm, characteristic of anatase and rutile phases of TiO_2, as can be seen in Fig. 3. Platinum nanoparticles induce broad adsorption over the entire visible region. These results agree with previous studies[58,59] and show the plasmon-induced enhancement of absorption from the Pt cluster on the TiO_2 surface.

The influence of Pt loading on TiO_2 for hydrogen production was studied using CMC-Na as a sacrificial agent. Fig. 4a shows the performance of TiO_2 as a function of Pt deposited. As expected H_2 production was negligible when no Pt was involved, and no signal could be detected, showing that Pt has a catalytic role for hydrogen evolution during the photocatalytic process. When the amount of Pt loading was 0.2% and 0.5%, outstanding improvement can be noticed. However, when 1% Pt was dispersed on the photocatalyst surface, only a marginal improvement was observed when the production was compared with H_2 obtained by using 0.5% Pt nanocomposites. Higher Pt contents could lead to the agglomeration of Pt NPs, and the incorporation of excessive metal sites may increase the electron–hole recombination due to an increase in the free electron density.[60] It is also possible to form aggregates over time, generating a shading effect from the agglomerate suspended particles diminishing light penetration. To verify the role of Pt on TiO_2, the obtained photogenerated $^{\bullet}OH$ was studied by PL spectroscopy using terephthalic acid (TPA) as a scavenger. It is well known that TPA reacts with $^{\bullet}OH$ radicals producing 2-hydroxy terephthalic acid (hTPA),[61,62] which has an emission peak around 432 nm when is excited with a 323 nm light source. Fig. 4b shows the hTPA concentration calculated from PL intensity at 432 nm (see Table S1†) and the calibration curve is presented in Fig. S1.† hTPA concentration of TPA solution gradually increased over irradiation time with the lowest concentration corresponding to bare TiO_2, increasing proportionately with Pt loading. This implies that the amount of $^{\bullet}OH$ generated is more significant when Pt is present in the photocatalyst following the order 1Pt–TiO_2 > 0.5Pt–TiO_2 > 0.2Pt–TiO_2 > TiO_2. This result confirms that Pt acts by suppressing the recombination of the hole–electron pair and thus improves the $^{\bullet}OH$ generation at the same time. Even though 1% Pt loading presents higher $^{\bullet}OH$ production, the agglomeration of Pt NPs may increase the electron–hole pair recombination making the charge separation more difficult, during the photocatalytic process. From these results, we decided to carry out all the photocatalytic hydrogen production tests using 0.5Pt–TiO_2 as the photocatalyst.

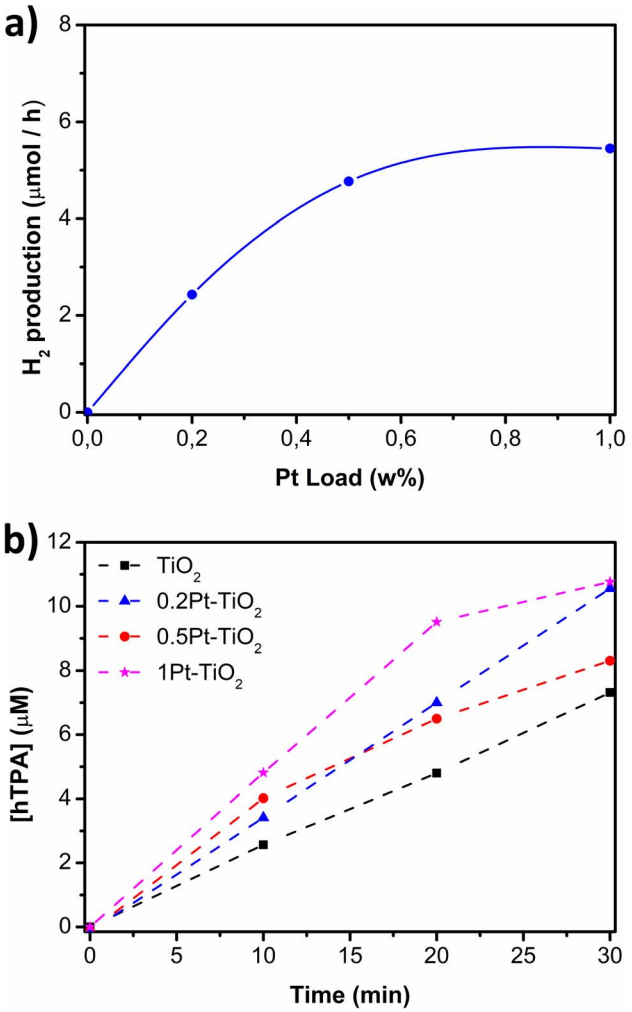

Fig. 4 (a) Hydrogen production according to the Pt loading on TiO_2 photocatalyst, (b) 2-hydroxy terephthalic acid concentration (hTPA) produced during 30 min of irradiation for bared TiO_2, 0.2 wt% of Pt loaded on TiO_2 (0.2Pt–TiO_2), 0.5 wt% of Pt loaded on TiO_2 (0.5Pt–TiO_2) and 1 wt% of Pt loaded on TiO_2 (1Pt–TiO_2).

Photocatalytic hydrogen production using celluloses listed in Table 1 and the photocatalyst prepared with 0.5% Pt loading were compared. The production rates are shown in Fig. 5a and b. When no sacrificial agent was added, only water splitting contributing to the hydrogen production process is observed. This modest H_2 production improves when a sacrificial agent is added during the photocatalytic reaction. Cellulose extracted from rapeseed straw, either H_2O_2-bleached or un-bleached, showed lower performance for H_2 production. On the other

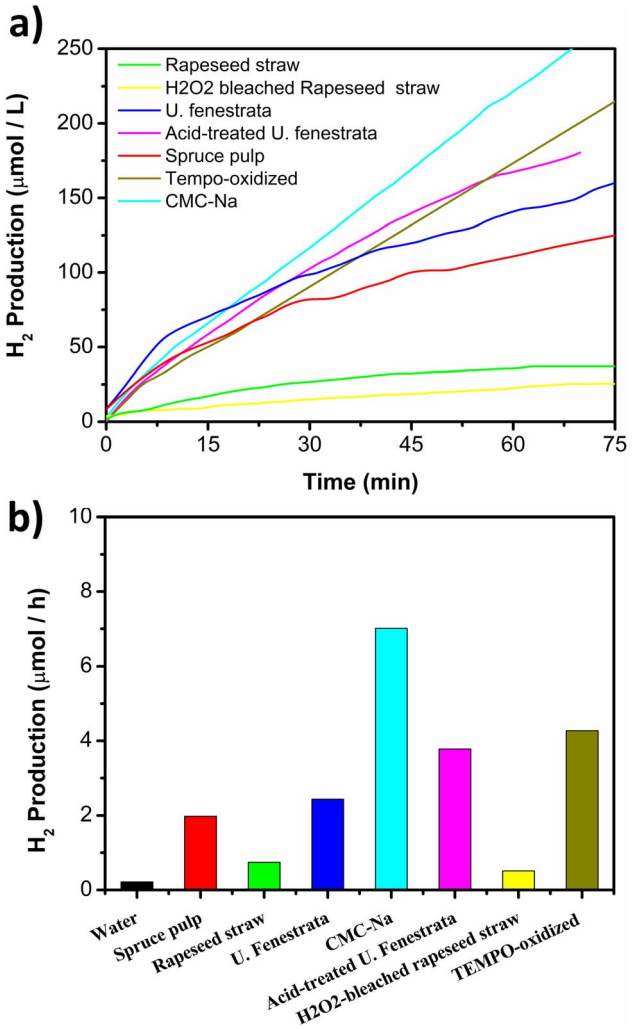

Fig. 5 (a) Hydrogen evolution measured *in situ* during the photocatalysis of celluloses extracted from rapeseed straw, H_2O_2-bleached cellulose extracted from rapeseed straw, α-cellulose spruce pulp, cellulose extracted from *U. fenestrata*, acid-treated cellulose extracted from *U. fenestrata* celluloses, and the cellulose derivatives CMC-Na and TEMPO-oxidized cellulose. (b) Hydrogen production per hour during the photo-reforming of different celluloses. The reactor corresponded to a 25 mL vessel, 0.3 mg mL^{-1} of photocatalyst and 0.25 mg mL^{-1} of sacrificial agent.

hand, CMC-Na and TEMPO-oxidized CNF exhibited the best hydrogen production rate. Comparing the crystallinity index (CI) between the different types of celluloses, it could be observed that lower CI led to increased H_2 production. Lower CI is associated with weaker chemical bonds,[63] and it has been found that during enzymatic hydrolysis of cellulose to glucose, for biofuel conversion, a completely amorphous sample is hydrolyzed faster than a partially crystalline cellulose.[64] A similar trend was reported by Caravaca *et al.* during cellulose reforming,[40] establishing that a CI of 80% or lower is the optimum value for fescue grass hydrolysis. Higher CI values lead to a difficult interaction between the photocatalyst particles and the interior sites of cellulose material. The smallest H_2 production was recorded with H_2O_2-bleached rapeseed straw cellulose. Before bleaching the rapeseed straw cellulose, the process includes an alkaline treatment where hemicelluloses, mainly xylan is mostly removed.[41] Removing these amorphous regions could lead to an increase in the crystallinity index and, subsequently, lead to a reduction in the hydrogen production rate.

From Fig. 5b, it is also possible to observe that lignin-free celluloses from green macroalgae, isolated from *U. fenestrata*, contributed to improved H_2 production. Lignin provides elasticity and mechanical strength to the cellulose microfibrils protecting them from chemical and enzymatic degradation.[65] Hence, lignin is likely to affect the interaction between the photocatalyst and cellulose, protecting the cellulose microfibrils and making it tougher to break and disperse, leading to an unstable suspension. Xyloglucan is partially soluble in water and interrupts the formation of cellulose crystals leading to a low CI.[66] This could explain the improved hydrogen production rate using *U. fenestrata* celluloses. However, a considerable difference in hydrogen production rate was found when the cellulose was acid-treated, increasing from 2.43 μmol h^{-1} for *U. fenestrata* to 3.78 μmol h^{-1} for acid-treated *U. fenestrata* cellulose. CI is higher for acid-treated *U. fenestrata* cellulose, however, so is the glucose content, which could improve the hydrogen production rate.[42] On the other hand, α-cellulose fibers from spruce pulp showed a lower performance with a production rate of 1.98 μmol h^{-1} despite containing 99% cellulose with no lignin, suggesting that the higher CI led to lower availability of cellulose as a sacrificial agent.

The total dispersion of completely water-insoluble cellulose is difficult to obtain because of the long rigid chains and the inter-molecular and intra-molecular forces that lead to an unstable system, as was the case of H_2O_2-bleached and unbleached cellulose extracted from rapeseed straw discussed above. Considering this, modification of cellulose structure to improve its water-solubility properties (widely discussed in the literature, see for instance[67–69]), where different groups substitute hydroxyl groups, could be beneficial in photocatalytic hydrogen production. Cellulose hydroxyl groups are substituted with carboxymethyl ($-CH_2-COO^-$) groups in CMC-Na and carboxylate ($RCOO^-$) groups in TEMPO-oxidized cellulose. The addition of these polar groups increases the solubility of cellulose, resulting in better suspension in aqueous media, and avoiding agglomeration and thus aggregation of the particles reducing its availability as an active component of the system. The degradation kinetics of cellulose is thus affected depending on the degree of substitution, the substitution pattern, and the degree of polymerization. Erdal *et al.* studied the degradation of CMC, establishing that the hydrolysis dramatically decreased when the degree of substitution was higher than 1.[70]

From the above, it is expected that using these cellulose derivatives as sacrificial agents will ameliorate hydrogen production. This is also clearly observed in Fig. 5b where CMC-Na and TEMPO-oxidized cellulose show the best performance for photocatalytic H_2 production with rates of 7.01 and 4.27 μmol h^{-1}, respectively. Meanwhile, Fig. 5a shows a pronounced hydrogen production slope when CMC-Na and TEMPO-oxidized cellulose were used. A similar trend was found during the first

minutes with acid-treated *U. fenestrata* cellulose and *U. fenestrata* cellulose. Zhao *et al.* reported that the photo-reforming of lignocellulose showed a similar pathway compared to the enzymatic oxidation processes,[71] where due to a kinetic factor of accessibility cellulose first is hydrolyzed into soluble glucose, formic acid, hydroxymethyl furfural (HMF), *etc.* These soluble products have faster diffusion rate consuming hydroxyl radicals that provide protons to the system,[72] which then get reduced to hydrogen gas. Fig. 6 corresponds to a schematic diagram showing different species involved in the degradation of the biomass samples. According to Machado *et al.*, hydroxyl radicals (˙OH) cause a structural fragmentation of lignin structure attacking the double bond of the aromatic rings.[73] On the other hand, hemicelluloses (like xyloglucan) and cellulose follow similar mineralization paths where ˙OH breaks the glycosidic linkages producing xylose and glucose, respectively. Xylose and glucose continue their degradation forming intermediates like arabinose, erythrose, galactose, glyceraldehyde, hydroxymethylfurfural (HMF), *etc.* until mineralization is complete and products like formic acid, carbon dioxide, carbon monoxide, and hydrogen are obtained.[74,75] This emphasizes the importance of ˙OH produced during the photocatalytic process as shown in Fig. 4b.

Based on the above discussions, the high activity observed during the first minutes when *U. fenestrata* and acid-treated *U. fenestrata* celluloses were used can be attributed to the consumption of the soluble xyloglucan present in their microstructure. Meanwhile, an induction period was observed before the H_2 production started when H_2O_2-bleached and unbleached celluloses extracted from rapeseed straw were used. Given the above observations, the performance of CMC-Na, Tempo-oxidized cellulose, *U. fenestrata*, and acid-treated *U. fenestrata* were compared with the performance of classical sacrificial agents keeping the concentration of photocatalyst constant with 0.3 mg mL^{-1} and 0.25 mg mL^{-1} sacrificial agent used, respectively. Sodium sulfide (Na_2S) and commercial glucose were considered for this comparison. From Fig. 7, it is possible to observe that glucose improves hydrogen yield when *U. fenestrata* and acid-treated *U. fenestrata* samples were considered, which is attributed to the glucose content in the acid-treated *U. fenestrata* mentioned above. On the other hand, Na_2S was used as an inorganic sacrificial agent presenting a different reaction mechanism than glucose, where Na_2S is more easily oxidizable as direct interaction with the holes generated on the photocatalyst[76,77] can occur, producing S_2^{2-} ions thus reducing the need of the presence of ˙OH radicals. Despite this, the performance of Na_2S is similar to CMC-Na which can be attributed to its high substitution degree of around 0.8 making it highly soluble showing its potential to be used as a biomass sacrificial agent.

The influence of the sacrificial agent concentration during photocatalysis was tested for CMC-Na by keeping the photocatalyst concentration constant at 0.3 mg mL^{-1}. Several suspensions were prepared between 0.25 and 5 mg mL^{-1}. From Fig. 8a, we can observe that the optimum cellulose concentration corresponds to 2.5 mg mL^{-1}. Higher cellulose concentrations showed a rapid decrease in H_2 production attributed to an increase in the shadowing effect of photocatalysis particles by

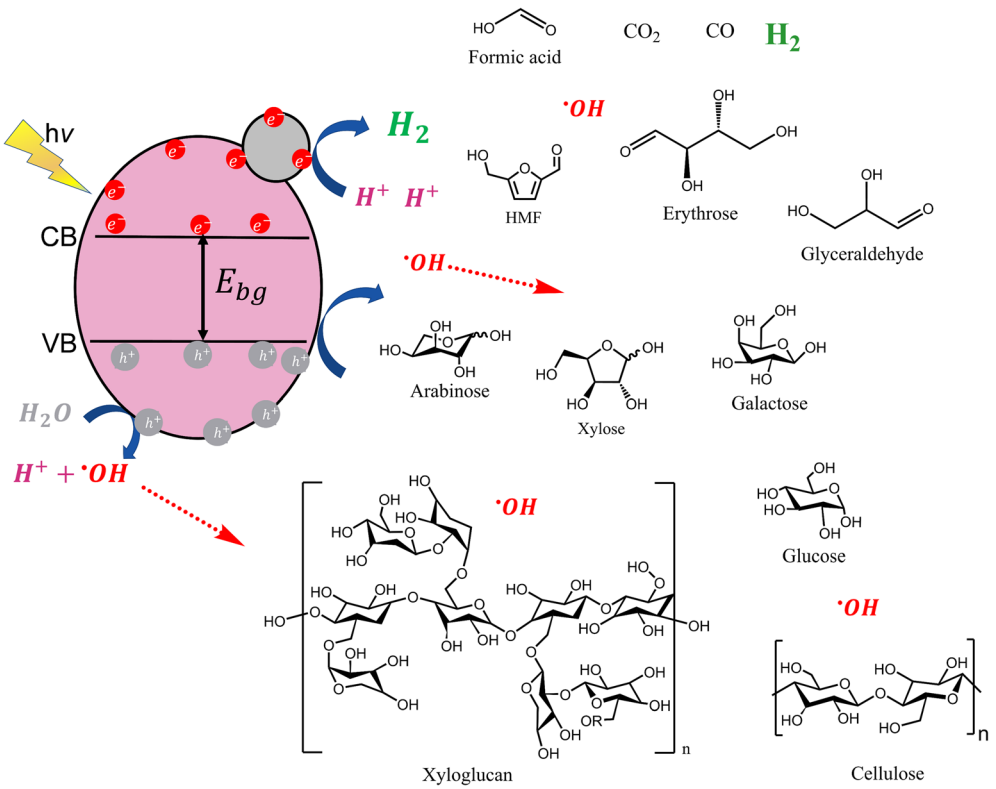

Fig. 6 Schematic representation of cellulose and hemicellulose degradation and molecules participating during the photocatalysis process.

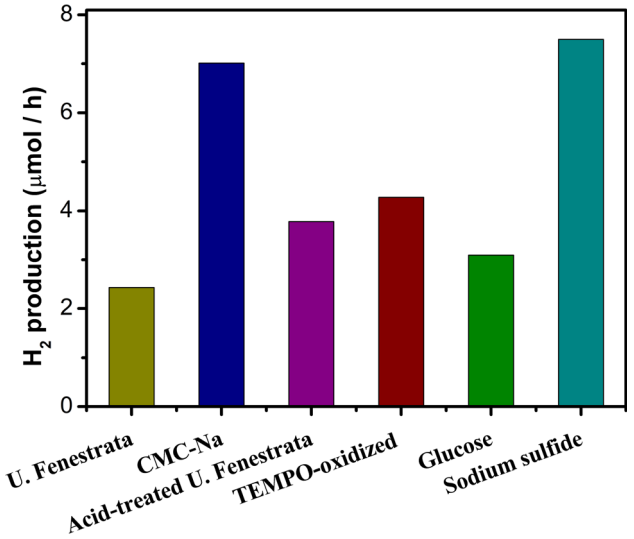

Fig. 7 Photocatalytic H_2 production of 0.5Pt–TiO_2 using different sacrificial agents.

the cellulose particles reducing the interaction of photons used for the generation of photoexcited electrons and holes on the semiconductor surface.

To study the influence of pH on the hydrogen production rates, different CMC-Na suspensions were prepared with pH from 2 to 5 and tested using 0.3 mg mL^{-1} of 0.5Pt–TiO_2 and 0.25 mg mL^{-1} of CMC-Na. From Fig. 8b, it is possible to notice an increase in H_2 production moving from pH 5 to pH 4, and the maximum output was recorded at pH 2. These results suggest that acidic pH is beneficial for the system's performance. This can be attributed to the presence of excess protons in the system lowering the overpotential needed for hydrogen evolution. However, at pH 2–3, the suspension was unstable, and agglomeration of particles occur. Even though the hydrogen production at pH 2 was almost double what was obtained at pH 5, the agglomeration became more severe with time, and the hydrogen production practically stopped due to the precipitation of the sacrificial agent together with the corrosion of the photocatalysts.[78] To explain the instability of the solution, the zeta potential values of CMC-Na were measured and are shown in Fig. S5.† From these results obtained at pH 2 and 3, particles have a net charge close to 0, making the suspension unstable thus enabling agglomeration. On the other hand, when the pH is higher than 4, the zeta potential values are more negative, decreasing the tendency of the agglomeration of the particles.

Long-term performance and recovery of the photocatalyst were studied considering 4 running cycles of 8 hours each, 2.5 mg mL^{-1} of CMC-Na was renewed in each cycle run, and 0.3 mg L^{-1} of 0.5Pt–TiO_2 was continuously recovered. Fig. 9 shows a linear tendency in the hydrogen production rate during the 8 h of light exposure. When subsequent other runs were performed the H_2 production remained stable during the first two cycles where only 10% of the capacity was reduced after 16 hours. Nevertheless, after the second run photocatalyst presented a significant decrease in the H_2 production rate of

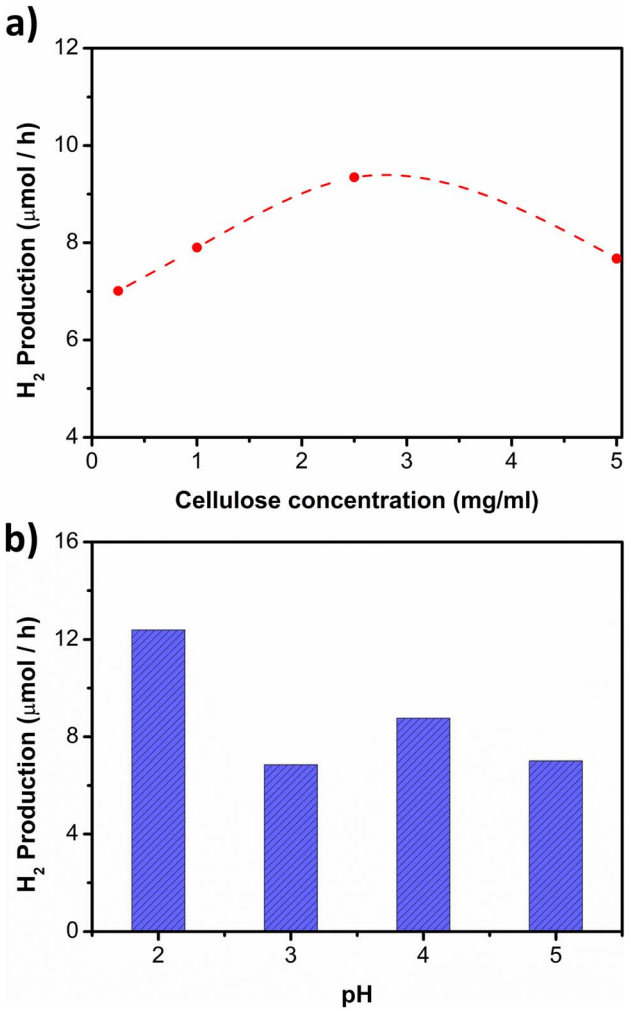

Fig. 8 (a) Hydrogen production regarding the concentration of CMC-Na, and (b) hydrogen production performance tested in a solution of 0.3 mg mL^{-1} of 0.5Pt–TiO_2 and 0.25 mg L^{-1} of CMC-Na at different pH.

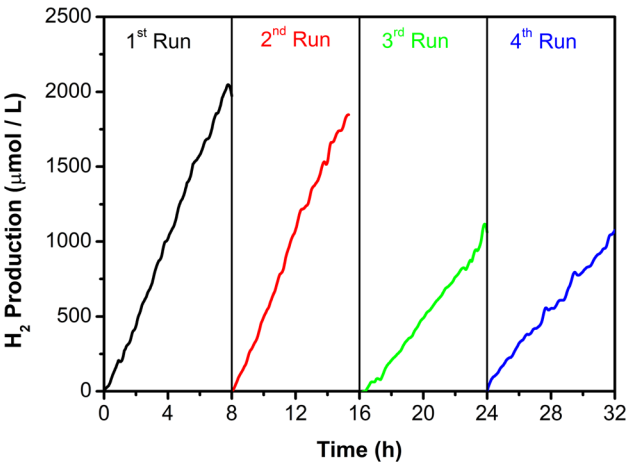

Fig. 9 Long-term stability and recyclability of the 0.5Pt–TiO_2 photocatalyst using CMC-Na as sacrificial agent.

approximately of 46% which kept constant in run 4. The instability associated with H_2 production it was related to incomplete biomass degradation and difficulties in recovering the photocatalyst at the end of every cycle run.

4. Conclusions

This work investigated photocatalytic hydrogen production by using different cellulose types as sacrificial agents using platinum loaded on TiO_2 as a photocatalyst. It was demonstrated that hydrogen could successfully be produced using all the cellulosic biomass and cellulose derivatives tested, and its performance is strongly related to the composition of the biomass used and the amount of platinum loading. Optimal performance towards H_2 production was obtained when 0.5 wt% of platinum was loaded. Hydrogen production was strongly affected by the crystallinity index and the presence of soluble structures, like xyloglucan in the cellulosic material which is consumed during the first minutes of the photocatalytic process. Lignin-free celluloses from green macroalgae, isolated from *U. fenestrata* algae was the best sacrificial agent showing a hydrogen production rate of 140.85 μmol L^{-1} that could be further improved in the cellulose obtained from *U. fenestrata* was acid-treated yielding 167.44 μmol L^{-1} hydrogen in 1 hour of exposure. Cellulose derivatives with incorporated polar substituents showed almost two times higher hydrogen production rates than the un-modified ones. The enhancement in the performance was associated with the higher solubility of the derivative products due to the carboxymethyl ($-CH_2-COO^-$) and carboxylate ($RCOO^-$) groups, improving the dispersion and the stability of the system when the pH was 5. A successful deployment of photocatalytic generation of H_2 from cellulose would have several positive effects associated with some relevant Sustainable Development Goals. Possible issues may arise when it comes to the photocatalyst used, which should allow good efficiency while being affordable enough, without posing any significant environmental threat throughout all its life cycle.

Conflicts of interest

There are no conflicts to declare.

Acknowledgements

MI Alvarado-Ávila would like to thank the National Commission for Scientific and Technological Research (ANID) for the Doctoral scholarship "Beca Chile" 2018-72190683. The authors also want to acknowledge partial financial support from Swedish Energy Agency (Energimyndigheten) through a project entitled HESAC (Project No. 45504-1).

References

1 IEA, *Global Energy Review 2021*, IEA, Paris, 2021.
2 *bp, Statistical Review of World Energy*, 2022, **https://www.bp.com/content/dam/bp/business-sites/en/global/corporate/pdfs/energy-economics/statistical-review/bp-stats-review-2022-full-report.pdf**.
3 S. Atilhan, S. Park, M. M. El-Halwagi, M. Atilhan, M. Moore and R. B. Nielsen, *Curr. Opin. Chem. Eng.*, 2021, **31**, 100668.
4 B. Khandelwal, A. Karakurt, P. R. Sekaran, V. Sethi and R. Singh, *Prog. Aeronaut. Sci.*, 2013, **60**, 45–59.
5 A. M. Oliveira, R. R. Beswick and Y. Yan, *Curr. Opin. Chem. Eng.*, 2021, **33**, 100701.
6 A. P. Simpson and A. E. Lutz, *Int. J. Hydrogen Energy*, 2007, **32**, 4811–4820.
7 S. Danwittayakul and J. Dutta, *Int. J. Hydrogen Energy*, 2012, **37**, 5518–5526.
8 S. Danwittayakul, K. Lakshman, S. Al-Harthi and J. Dutta, *Appl. Catal., A*, 2014, **471**, 63–69.
9 E. Kabir, P. Kumar, S. Kumar, A. A. Adelodun and K.-H. Kim, *Renewable Sustainable Energy Rev.*, 2018, **82**, 894–900.
10 A. Fujishima and K. Honda, *Nature*, 1972, **238**, 37–38.
11 X. Ning and G. Lu, *Nanoscale*, 2020, **12**, 1213–1223.
12 S. U. Khan, M. Al-Shahry and W. B. Ingler Jr, *Science*, 2002, **297**, 2243–2245.
13 F. Wang, C. Di Valentin and G. Pacchioni, *J. Phys. Chem. C*, 2012, **116**, 8901–8909.
14 K.-S. Mun, S. D. Alvarez, W.-Y. Choi and M. J. Sailor, *ACS Nano*, 2010, **4**, 2070–2076.
15 F. Loosli, P. Le Coustumer and S. Stoll, *Sci. Total Environ.*, 2015, **535**, 28–34.
16 B. S. Vadlamani, T. Uppal, S. C. Verma and M. Misra, *Sensors*, 2020, **20**, 5871.
17 S. Sarkar, A. Makhal, T. Bora, S. Baruah, J. Dutta and S. K. Pal, *Phys. Chem. Chem. Phys.*, 2011, **13**, 12488–12496.
18 S. Akel, R. Dillert, N. O. Balayeva, R. Boughaled, J. Koch, M. El Azzouzi and D. W. Bahnemann, *Catalysts*, 2018, **8**, 647.
19 S. Sarkar, A. Makhal, K. Lakshman, T. Bora, J. Dutta and S. Kumar Pal, *J. Phys. Chem. C*, 2012, **116**, 14248–14256.
20 J. Ran, J. Zhang, J. Yu, M. Jaroniec and S. Z. Qiao, *Chem. Soc. Rev.*, 2014, **43**, 7787–7812.
21 T. Bora, H. H. Kyaw and J. Dutta, *Electrochim. Acta*, 2012, **68**, 141–145.
22 T. Bora, H. H. Kyaw, S. Sarkar, S. K. Pal and J. Dutta, *Beilstein J. Nanotechnol.*, 2011, **2**, 681–690.
23 S. Kumar, F. Ye, B. Mazinani, S. Dobretsov and J. Dutta, *Int. J. Mol. Sci.*, 2021, **22**, 4513.
24 M. Batvandi, A. Haghighatzadeh, B. Mazinani and J. Dutta, *Appl. Phys. A: Mater. Sci. Process.*, 2022, **128**, 853.
25 X. Cai, Z. Zeng, Y. Liu, Z. Li, X. Gu, Y. Zhao, L. Mao and J. Zhang, *Appl. Catal., B*, 2021, **297**, 120391.
26 J. Velázquez, R. Fernández-González, L. Díaz, E. P. Melián, V. Rodríguez and P. Núñez, *J. Alloys Compd.*, 2017, **721**, 405–410.
27 A. Makhal, S. Sarkar, T. Bora, S. Baruah, J. Dutta, A. Raychaudhuri and S. K. Pal, *Nanotechnology*, 2010, **21**, 265703.
28 H. Tian, S.-Z. Kang, X. Li, L. Qin, M. Ji and J. Mu, *Sol. Energy Mater. Sol. Cells*, 2015, **134**, 309–317.
29 G. L. Chiarello, M. H. Aguirre and E. Selli, *J. Catal.*, 2010, **273**, 182–190.

30 S. E. Hosseini, M. Abdul Wahid, M. Jamil, A. A. Azli and M. F. Misbah, *Int. J. Energy Res.*, 2015, **39**, 1597–1615.
31 S. Su, W. Li, Z. Bai, H. Xiang and J. Bai, *Int. J. Hydrogen Energy*, 2010, **35**, 4459–4465.
32 Y.-C. Lo, M.-D. Bai, W.-M. Chen and J.-S. Chang, *Bioresour. Technol.*, 2008, **99**, 8299–8303.
33 J. Zou, H. Yang, Z. Zeng, C. Wu, P. T. Williams and H. Chen, *Int. J. Hydrogen Energy*, 2016, **41**, 10598–10607.
34 A. M. Balu and R. Luque, in *Producing Fuels and Fine Chemicals from Biomass Using Nanomaterials*, 2013, pp. 1–4.
35 S. Siahrostami, G.-L. Li, V. Viswanathan and J. K. Nørskov, *J. Phys. Chem. Lett.*, 2017, **8**, 1157–1160.
36 G. Zhang, C. Ni, X. Huang, A. Welgamage, L. A. Lawton, P. K. Robertson and J. T. Irvine, *Chem. Commun.*, 2016, **52**, 1673–1676.
37 D. W. Wakerley, M. F. Kuehnel, K. L. Orchard, K. H. Ly, T. E. Rosser and E. Reisner, *Nat. Energy*, 2017, **2**, 1–9.
38 C. Chang, N. Skillen, S. Nagarajan, K. Ralphs, J. T. Irvine, L. Lawton and P. K. Robertson, *Sustainable Energy Fuels*, 2019, **3**, 1971–1975.
39 A. Speltini, M. Sturini, D. Dondi, E. Annovazzi, F. Maraschi, V. Caratto, A. Profumo and A. Buttafava, *Photochem. Photobiol. Sci.*, 2014, **13**, 1410–1419.
40 A. Caravaca, W. Jones, C. Hardacre and M. Bowker, *Proc. R. Soc. A*, 2016, **472**, 20160054.
41 A. Svärd, R. Moriana, E. Brännvall and U. Edlund, *ACS Sustainable Chem. Eng.*, 2018, **7**, 790–801.
42 N. Wahlström, U. Edlund, H. Pavia, G. Toth, A. Jaworski, A. J. Pell, F. X. Choong, H. Shirani, K. P. R. Nilsson and A. Richter-Dahlfors, *Cellulose*, 2020, **27**, 3707–3725.
43 A. Isogai, T. Saito and H. Fukuzumi, *Nanoscale*, 2011, **3**, 71–85.
44 W. Yao, J. Yang, J. Wang and Y. Nuli, *Electrochem. Commun.*, 2007, **9**, 1029–1034.
45 R. A. Al-Alawi, K. Laxman, S. Dastgir and J. Dutta, *Appl. Surf. Sci.*, 2016, **377**, 200–206.
46 M. I. A. Ávila, E. Toledo-Carrillo and J. Dutta, *Clean. Eng. Technol.*, 2020, **1**, 100016.
47 K. Nisizawa, *J. Ferment. Technol.*, 1973, **51**, 267–304.
48 H. Ma, B. Yin, S. Wang, Y. Jiao, W. Pan, S. Huang, S. Chen and F. Meng, *ChemPhysChem*, 2004, **5**, 68–75.
49 Z. Cao, T. Zhang, P. Ren, D. Cao, Y. Lin, L. Wang, B. Zhang and X. Xiang, *Catalysts*, 2020, **10**, 69.
50 G. Konecoglu, T. Safak, Y. Kalpakli and M. Akgun, *Adv. Environ. Res.*, 2015, **4**, 25–38.
51 E. Drzymała, G. Gruzeł, A. Pajor-Świerzy, J. Depciuch, R. Socha, A. Kowal, P. Warszyński and M. Parlinska-Wojtan, *J. Nanopart. Res.*, 2018, **20**, 1–13.
52 G. Marzun, C. Streich, S. Jendrzej, S. Barcikowski and P. Wagener, *Langmuir*, 2014, **30**, 11928–11936.
53 H.-S. Oh, J.-G. Oh, Y.-G. Hong and H. Kim, *Electrochim. Acta*, 2007, **52**, 7278–7285.
54 A. Srivastava, M. Deepa, S. Bhandari and H. Fuess, *Nanoscale Res. Lett.*, 2009, **4**, 54–62.
55 R. A. Spurr and H. Myers, *Anal. Chem.*, 1957, **29**, 760–762.
56 S. Oh, H. Ha, H. Choi, C. Jo, J. Cho, H. Choi, R. Ryoo, H. Y. Kim and J. Y. Park, *J. Chem. Phys.*, 2019, **151**, 234716.
57 T. Bora, K. K. Lakshman, S. Sarkar, A. Makhal, S. Sardar, S. K. Pal and J. Dutta, *Beilstein J. Nanotechnol.*, 2013, **4**, 714–725.
58 L. M. Ahmed, I. Ivanova, F. H. Hussein and D. W. Bahnemann, *Int. J. Photoenergy*, 2014, **2014**, 503516.
59 L. Hou, M. Zhang, Z. Guan, Q. Li and J. Yang, *J. Nanopart. Res.*, 2018, **20**, 1–8.
60 P. Pichat, J. M. Herrmann, J. Disdier, M. N. Mozzanega and H. Courbon, in *Studies in Surface Science and Catalysis*, ed. S. Kaliaguine and A. Mahay, Elsevier, 1984, vol. 19, pp. 319–326.
61 W. Dong, D. Wang, L. Jiang, H. Zhu, H. Huang, J. Li, H. Zhao, C. Li, B. Chen and G. Deng, *Mater. Lett.*, 2013, **98**, 265–268.
62 S. E. Page, W. A. Arnold and K. McNeill, *J. Environ. Monit.*, 2010, **12**, 1658–1665.
63 S. Park, J. O. Baker, M. E. Himmel, P. A. Parilla and D. K. Johnson, *Biotechnol. Biofuels*, 2010, **3**, 10.
64 M. Hall, P. Bansal, J. H. Lee, M. J. Realff and A. S. Bommarius, *FEBS J.*, 2010, **277**, 1571–1582.
65 S. I. Mussatto and J. A. Teixeira, *Current Research. Technology and Education Topics in Applied Microbiology and Microbial Biotechnology*, ed. A. Méndez-Vilas, 2010, vol. 2, pp. 897–907, **https://hdl.handle.net/1822/16762**.
66 Q. Zhou, M. W. Rutland, T. T. Teeri and H. Brumer, *Cellulose*, 2007, **14**, 625–641.
67 S. Schmidt, T. Liebert and T. Heinze, *Green Chem.*, 2014, **16**, 1941–1946.
68 C. T. O'Brien, T. Virtanen, S. Donets, J. Jennings, O. Guskova, A. H. Morrell, M. Rymaruk, L. Ruusuvirta, J. Salmela and H. Setala, *Polymer*, 2021, **223**, 123681.
69 S. Thiangtham, J. Runt and H. Manuspiya, *Carbohydr. Polym.*, 2019, **208**, 314–322.
70 N. B. Erdal and M. Hakkarainen, *Biomacromolecules*, 2022, **23**, 2713–2729.
71 H. Zhao, C.-F. Li, X. Yu, N. Zhong, Z.-Y. Hu, Y. Li, S. Larter, M. G. Kibria and J. Hu, *Appl. Catal., B*, 2022, **302**, 120872.
72 H. Hao, L. Zhang, W. Wang and S. Zeng, *ChemSusChem*, 2018, **11**, 2810–2817.
73 A. E. H. Machado, A. M. Furuyama, S. Z. Falone, R. Ruggiero, D. d. S. Perez and A. Castellan, *Chemosphere*, 2000, **40**, 115–124.
74 R. Chong, J. Li, Y. Ma, B. Zhang, H. Han and C. Li, *J. Catal.*, 2014, **314**, 101–108.
75 H. Zhao, X. Yu, G. Hu, N. Zhong, Z.-Y. Hu, S. Larter, Y. Li, M. G. Kibria and J. Hu, *Green Chem.*, 2021, **23**, 8124–8130.
76 C. Li, H. Wang, J. Ming, M. Liu and P. Fang, *Int. J. Hydrogen Energy*, 2017, **42**, 16968–16978.
77 X. Li, J. Xu, L. Li, S. Zhao, M. Mao, Z. Liu and Y. Li, *Catal. Lett.*, 2021, **151**, 2408–2419.
78 M. Wang, S. Shen, L. Li, Z. Tang and J. Yang, *J. Mater. Sci.*, 2017, **52**, 5155–5164.